

Adaptation in Living Systems

Yuhai Tu¹ and Wouter-Jan Rappel²¹IBM T.J. Watson Research Center, Yorktown Heights, New York 10598, USA;
email: yuhai@us.ibm.com²Department of Physics, University of California, San Diego, La Jolla, California 92093, USA;
email: rappel@physics.ucsd.edu

Annu. Rev. Condens. Matter Phys. 2018.
9:183–205

First published as a Review in Advance on
December 8, 2017

The *Annual Review of Condensed Matter Physics* is
online at conmatphys.annualreviews.org

<https://doi.org/10.1146/annurev-conmatphys-033117-054046>

Copyright © 2018 by Annual Reviews.
All rights reserved

Keywords

biochemical network, dynamics, nonequilibrium, molecular mechanism, modeling, chemotaxis, gradient sensing

Abstract

Adaptation refers to the biological phenomenon where living systems change their internal states in response to changes in their environments in order to maintain certain key functions critical for their survival and fitness. Adaptation is one of the most ubiquitous and arguably one of the most fundamental properties of living systems. It occurs throughout all biological scales, from adaptation of populations of species over evolutionary time to adaptation of a single cell to different environmental stresses during its life span. In this article, we review some of the recent progress made in understanding molecular mechanisms of cellular-level adaptation. We take the minimalist (or the physicist) approach and study the simplest systems that exhibit generic adaptive behaviors, namely chemotaxis in bacterium cells (*Escherichia coli*) and eukaryotic cells (*Dictyostelium*). We focus on understanding the basic biochemical interaction networks that are responsible for adaptation dynamics. By combining theoretical modeling with quantitative experimentation, we demonstrate universal features in adaptation as well as important differences in different cellular systems. Future work in extending the modeling framework to study adaptation in more complex systems such as sensory neurons is also discussed.

1. INTRODUCTION

Living systems, from a single cell to multicellular organisms and populations of interacting species, all have the amazing ability to adapt to changes in their environments. Adaptation allows living systems to adjust themselves in response to persistent changes of the environment. At the evolutionary timescale, adaptation allows species to evolve driven by changes in the environment. At the timescale of the life span of a living system, the ability to adapt is critical for the system's survival by maintaining its homeostasis under different environmental conditions. At the even shorter timescale of individual signaling pathways, such as those for sensory signal transduction, adaptation can greatly extend the range of sensitive detection and provides a way to compute/process environmental information.

What are the possible mechanisms for adaptation in living systems? Are there any universal principles governing interactions of the underlying living matter (biomolecules, cells, organisms) that are responsible for the vast variety of adaptive behaviors in biology? Are there any fundamental limitations to the performance of adaptation?

In this review, we examine some of the recent developments in addressing these questions by combining theoretical analysis, computational modeling, and quantitative experiments for representative sensory signaling systems, including bacterium cells (*Escherichia coli*) and eukaryotic cells (*Dictyostelium discoideum*). We first present a general mathematical framework for studying adaptation dynamics. Next, we study two distinct biochemical networks for adaptation and the corresponding biological systems that employ these networks. We then investigate the universal properties of adaptation independent of the specific network structure. We conclude by outlining some of the remaining challenges for future investigations.

2. ADAPTATION AS A DYNAMICAL SYSTEM: A MATHEMATICAL FRAMEWORK

We present a general mathematical framework under which we may study adaptation. We denote $X(t)$ as the input (stimulus strength) and $Z(t)$ as the output of the biochemical network, where t is time. A change in X results in a change in Z with a fast response time. The output also depends on a slower internal variable $Y(t)$, which depends on X , Y , and Z . The system can be described by two generic dynamical equations:

$$\begin{aligned}\frac{dZ}{dt} &= G(X, Y, Z), \\ \frac{dY}{dt} &= F(X, Y, Z),\end{aligned}\tag{1}$$

where F and G are the rate functions for Y and Z , respectively.

The nullclines from $dZ/dt = 0$ and $dY/dt = 0$ are given by $Z = g(Y, X)$ and $Y = f(Z, X)$, respectively. The steady-state solution for a fixed X is determined by the intercept of the two nullclines. Here, we express the steady-state solution as $Y = Y_s(X)$ and $Z = Z_s(X)$. A typical adaptive response is shown in **Figure 1a**. Upon a sudden increase of the input from X to $X + \Delta X$, the output Z first changes from $Z_s(X)$ to a peak value of $Z_p(X + \Delta X, X)$ before recovering (adapting) to its new steady-state value $Z_s(X + \Delta X)$ at a longer time. In the following, we describe the basic requirements for adaptation and its characterization.

2.1. Separation of Timescales

We can define two timescales $\tau_Z \equiv -(\frac{\partial G}{\partial Z})^{-1}$ and $\tau_Y \equiv -(\frac{\partial F}{\partial Y})^{-1}$, which characterize the timescales for response and adaptation, respectively. To have a high sensitivity to a sudden change in its

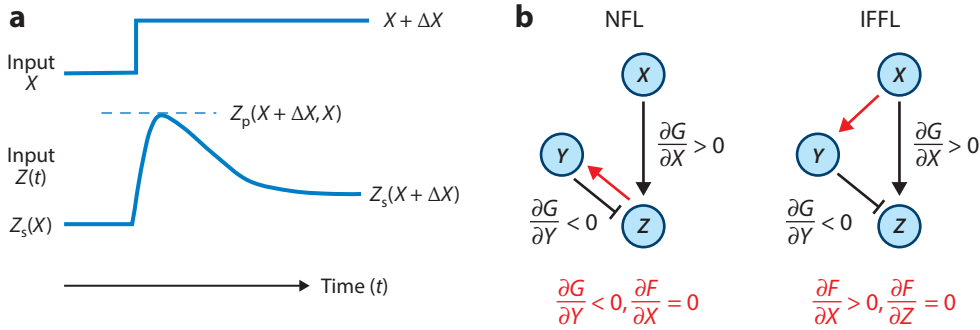


Figure 1

Generic adaptation behavior and responsible network motifs. (a) Illustration of adaptation dynamics of the output $Z(t)$ in response to a step function change in input from X to $X + \Delta X$. (b) The two basic network architectures (motifs) that can provide accurate adaptation. The red arrow lines highlight the slow interactions critical for adaptation. The NFL and IFFL networks differ in the placement of these slow interactions. Abbreviations: IFFL, incoherent feed-forward loop; NFL, negative feedback loop.

environment, a cell needs to first respond quickly. To maintain the high sensitivity over a wide range of backgrounds, the cell needs to adapt to a constant environment over a longer timescale. Indeed, one of the key requirements for adaptation is the separation of these two timescales, i.e., $\tau_Z \ll \tau_Y$. This means that the controller Y adjusts the system only after the system has enough time to respond. Due to its slow timescale, Y can also be understood as a working memory for the signal encountered by the cell.

2.2. Response Sensitivity and Adaptation Accuracy

There are two key characteristics for adaptation. The short time response is characterized by the response sensitivity:

$$S \equiv \frac{|Z_p(X + \Delta X, X) - Z_s(X)|}{|\Delta X|} \quad 2.$$

for small ΔX . The long time recovery is characterized by the adaptation error:

$$\epsilon \equiv \frac{|Z_s(X + \Delta X) - Z_s(X)|}{|Z_p(X + \Delta X, X) - Z_s(X)|}, \quad 3.$$

which measures how close the output adapts back to its original value relative to the initial response. Adaptive behavior requires $\epsilon < 1$, and perfect adaptation corresponds to $\epsilon = 0$ when the adapted output recovers to exactly its prestimulus value.

2.3. Network Requirement for Adaptation

Given the separation of timescales $\tau_Z \ll \tau_Y$, the short time response Z_p can be expressed as $Z_p(X + \Delta X, X) \approx g[Y_s(X), X + \Delta X]$. For small $|\Delta X|$, we can express the initial response as $|Z_p(X + \Delta X, X) - Z_s(X)| \approx |g[Y_s(X), X + \Delta X] - g[Y_s(X), X]| = |\frac{\partial g}{\partial X} \Delta X|$ and the adapted response as $|Z_s(X + \Delta X) - Z_s(X)| = |g[Y_s(X + \Delta X), X + \Delta X] - g[Y_s(X), X]| = |(\frac{\partial g}{\partial X} + \frac{\partial g}{\partial Y} \times \frac{dY_s}{dX}) \Delta X|$. Plugging these expressions into Equation 3, the requirement $\epsilon < 1$ results in a necessary condition for adaptation:

$$\frac{\partial g}{\partial X} \times \left(\frac{\partial g}{\partial Y} \times \frac{dY_s}{dX} \right) < 0. \quad 4.$$

The above requirement for adaptation has a simple intuitive interpretation: Adaptation requires the two pathways from input to output—one direct ($\frac{\partial g}{\partial X}$) and one indirect through Y ($\frac{\partial g}{\partial Y} \times \frac{dY_s}{dX}$)—to have opposite signs, i.e., one excitatory and the other inhibitory.

2.4. Two Basic Network Motifs for Adaptation

Without losing generality, we investigate the case $\frac{\partial g}{\partial X} > 0$ and $\frac{\partial g}{\partial Y} < 0$. It is straightforward to show that the other case in which $\frac{\partial g}{\partial X} < 0$ and $\frac{\partial g}{\partial Y} > 0$ works similarly. From Equation 4, we obtain the condition for adaptation:

$$\frac{dY_s}{dX} = \frac{\frac{\partial f}{\partial X} + \frac{\partial f}{\partial Z} \frac{\partial g}{\partial X}}{1 - \frac{\partial f}{\partial Z} \frac{\partial g}{\partial Y}} \approx \frac{\partial f}{\partial X} + \frac{\partial f}{\partial Z} \frac{\partial g}{\partial X} > 0, \quad 5.$$

where the last approximation was obtained by using $\frac{\partial f}{\partial Z} \frac{\partial g}{\partial Y} \propto \tau_Z/\tau_Y \ll 1$.

This adaptation condition is satisfied by two basic networks with a minimum number of nonzero interactions: (a) $\partial f/\partial Z > 0$, $\partial f/\partial X = 0$, and (b) $\partial f/\partial X > 0$, $\partial f/\partial Z = 0$. As illustrated in **Figure 1b**, the first network is called the negative feedback loop (NFL) network because of the negative feedback loop $Z \rightarrow Y \dashv Z$. The second network is called the incoherent feed-forward loop (IFFL) network because the loop is formed by two feed-forward paths, $X \rightarrow Z$ and $X \rightarrow Y \dashv Z$, with opposite (incoherent) signs. Indeed, an exhaustive search of all possible three-node networks found that the NFL and IFFL are the only two basic network motifs that enable strong response and accurate adaptation (1). In realistic biological systems, the dynamical variables are protein concentrations in different conformational states, and interactions are carried out by enzymatic reactions with multiple intermediate control elements (a vector \vec{Y}).

Due to their generality, the simple dynamical system model and the basic network structures (NFL and IFFL) provide a powerful framework to understand adaptation in a wide range of different cellular systems including *E. coli* and *Dictyostelium*, which we describe below.

3. ADAPTATION IN BACTERIAL CHEMOTAXIS

Due to its relative simplicity, *E. coli* chemotaxis has served as an important model system to study sensory adaptation. Berg & Brown first observed more than 40 years ago that upon a sudden increase in the concentration of chemoattractant aspartate, a cell's tumbling frequency initially decreases, then recovers, and eventually returns back to its prestimulus level (2). The adapted value of the tumbling frequency remains the same for a wide range of stimulus strengths (aspartate concentrations). This accurate adaptation is remarkable given the large variations in the concentrations of the key biomolecules among individual cells (3).

3.1. Molecular Mechanism

The quest for the molecular mechanism of adaptation motivated a large body of in-depth study into *E. coli* chemotaxis. The result is a quantitative understanding of the system.

3.1.1. Signal transduction. The bacterial chemotaxis signaling pathway has been well studied (see Reference 4 for a review on the signaling pathway). External chemical signals are sensed by the membrane-bound chemoreceptors in a bacterium cell such as *E. coli*. When chemoeffector molecules (ligands), such as amino acids and sugar molecules, bind with chemoreceptors, they induce conformational changes of the receptor, which in turn control the kinase activity of the cytosolic protein CheA. The chemoreceptors, histidine kinase CheA, and an adaptor protein

CheW form extended two-dimensional clusters with up to thousands of proteins in them (5). These receptor clusters, containing many directly and indirectly coupled receptors, are responsible for signal amplification in the system (see Reference 6 for a recent review on modeling). The activated CheA first autophosphorylates and then passes the phosphate group onto the response regulator proteins CheY and CheB. The phosphorylated CheY (CheY-P) can bind with the motor switch protein FliM to control the bacterial flagellar motor's rotational direction and thus the cell's motility. This constitutes the linear part of the signal transduction in bacterial chemotaxis.

3.1.2. Adaptation mechanism. The linear signal transduction pathway described above allows the cell to sense and respond. However, the range of stimulus concentrations over which a cell can respond is limited by the sensitivity range of the chemoreceptor, which is finite (less than one order of magnitude). The bacterial chemosensory system functions in an environment with a wide range of chemoeffector concentrations because of adaptation. We now know that at the molecular level, bacterial chemoreceptors adapt by covalent modification, i.e., methylation and demethylation of four specific amino-acid residues catalyzed by the enzymes CheR and CheB-P, respectively. Receptor adaptation dynamically adjusts its sensitive range according to the background and allows the receptor to detect changes in the environment using the most sensitive part of its response curve.

3.2. The Standard Model of Bacterial Chemotaxis

The state of a given receptor can be represented by three variables: its activity a , its ligand occupancy status l determined by the ligand concentration $[L]$, and its methylation level m . For a simple two-state (active and inactive) model for a receptor with five methylation levels and ligand binding status (ligand-bound and vacant), there are $2 \times 2 \times 5 = 20$ states with $4 \times 9 \times 2 = 72$ reactions among them. Mathematical models based on the transitions between these discrete states were used to study the dynamics and robustness of the system (7–9). Here, we use a simple coarse-grained model to describe the dynamics of the averaged properties of the system. Following the convention developed in the previous section, we define the output $Z \equiv \langle a \rangle$ and controller $Y \equiv \langle m \rangle$, which are both continuous variables. The input is the ligand concentration $X \equiv [L]$ (the correspondence between the different variables is summarized in **Table 1**). Below, we develop the simplest mathematical model for these averaged variables guided by separation of timescales and quantitative experiments.

3.2.1. Fast-response dynamics. For bacterial chemotaxis, both the ligand binding dynamics and kinase activity dynamics are faster than the receptor methylation process. Therefore, at a timescale faster than the methylation time, we can consider the dynamics of the output Z with a fixed Y :

$$\frac{dZ}{dt} = -[Z - g(Y, X)]/\tau_Z, \quad 6.$$

Table 1 Notational correspondence for bacterial and eukaryotic chemotaxis

This review	Bacterial chemotaxis	Eukaryotic chemotaxis
Input X	Ligand concentration $[L]$	Ligand concentration (R)
Internal Y	Methylation level m	Activator/Inhibitor (RasGEF, RasGAP)
Output Z	Receptor activity a	Output (RasGTP)

Abbreviations: RasGap, RasGTPase-activating protein; RasGEF, Ras guanine nucleotide exchange factor; RasGTP, Ras guanosine triphosphate.

where τ_Z is a fast timescale that depends on both the ligand binding and kinase activation dynamics. In steady state, we have $Z = g(Y, X)$. The functional form of $g(Y, X)$ can be determined experimentally by measuring the input–output relationship (Z versus X) in genetically engineered cells with a fixed value of Y (10, 11). Experimentally, this input–output relationship was found to follow a sigmoidal form with a large Hill coefficient. Theoretically, this input–output dependence can be explained by a Monod–Wyman–Changeux (MWC) model (11–13), for a large cluster of highly cooperative (all-or-none) receptors or by an Ising-type model in which receptors interact with their nearest neighbors in an extended lattice of receptors (14–16). The MWC model leads to a simple analytical result, which we use here:

$$g(Y, X) = \left[1 + e^{N f_m(Y)} \left(\frac{1 + X/K_i}{1 + X/K_a} \right)^N \right]^{-1}, \quad 7.$$

where N is the number of highly correlated receptors in the cluster and K_a and K_i are the dissociation constants for the active and inactive receptors, respectively, with $K_a \gg K_i$. The effects of receptor methylation are given by the free-energy difference $f_m(Y)$ between active and inactive states for a receptor that is not bound to the ligand. Experimental data reveals that this energy difference depends (roughly) linearly on Y : $f_m(Y) \approx -\alpha(Y - m_0)$, with $\alpha \approx 1.7$ (17, 18).

3.2.2. Slow-adaptation dynamics. From Equation 7, it is clear that varying Y shifts the sensitivity of the input–output response. How does the system adjust its receptor methylation level in response to changes in the environment to enable adaptation? Details of the enzymatic reactions (methylation and demethylation) and their kinetic rates are not well known. However, significant insights into the methylation dynamics were gained by the systems-level adaptation behavior. For *E. coli* chemotaxis, adaptation is highly accurate with an error $\epsilon \sim 1\text{--}4\%$; i.e., the adapted value of Z activity is independent of the input X and adaptation is nearly perfect. A simple way to achieve perfect adaptation is to have the methylation rate function F depend only on Z :

$$\frac{dY}{dt} = F(Z), \quad 8.$$

where F does not depend on Y and X explicitly. In steady state, we have $F(Z_s) = 0$, which results in an adapted activity $Z_s = F^{-1}(0)$ that is independent of the input X . This perfect adaptation mechanism is related to the integral control system in engineering (19).

For *E. coli* chemotaxis, receptor methylation increases kinase activity $\frac{\partial g}{\partial Y} > 0$, thus $\frac{dF(Z)}{dZ} < 0$ (at least near $Z = Z_s$) is required to maintain stability of the adapted state. Given that the interactions between the output (Z) and the controller (Y) have opposite signs $\frac{dF(Z)}{dZ} \times \frac{\partial g}{\partial Y} < 0$, it is clear that bacterial chemotaxis adaptation is carried out by a negative feedback loop (NFL) network. Combining the fast and slow dynamical equations, Equations 6 and 8 constitute the “standard model of bacterial chemotaxis” (20), which can be used to predict responses to arbitrary input signals (18, 21).

3.3. Comparison with Quantitative Experiments

One major recent advance in bacterial chemotaxis research was the Förster Resonance Energy Transfer (FRET) assay for studying *E. coli* chemotaxis signaling pathway in vivo. **Figure 2a** shows a typical response to a strong stimulus (10). These quantitative input–output measurements for wild-type (WT) cells as well as different mutants have been instrumental for model development. For simple step-function stimuli (addition and removal) as shown in **Figure 2a**, the standard model can be analyzed by using the nullcline analysis and exploiting the separation of timescales,

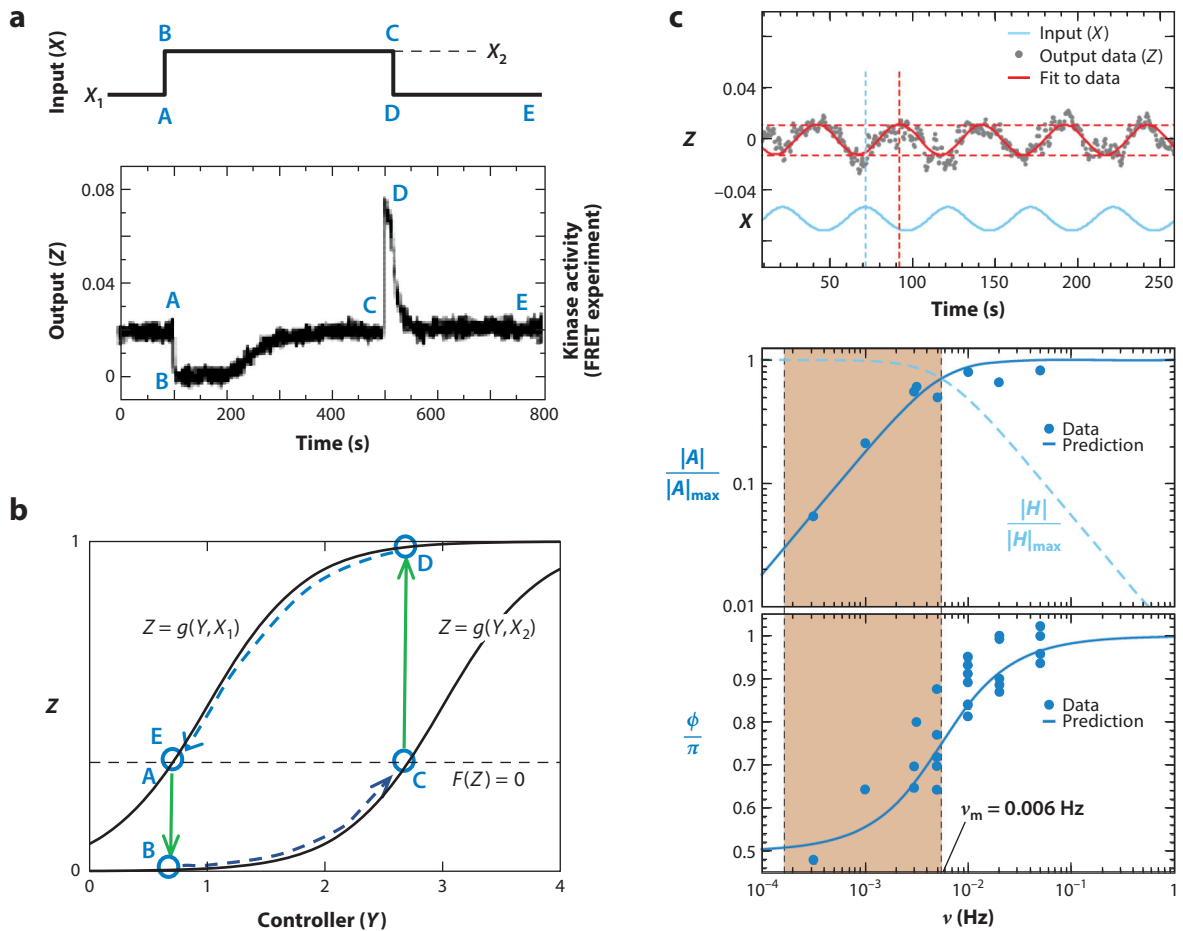


Figure 2

Comparison between predictions of the standard model of bacterial chemotaxis and quantitative experiments. (a) Response of *Escherichia coli* to step up and step down (addition and removal, respectively) of attractant MeAsp concentrations (X_1 and X_2). The response (kinase activity) is measured by using FRET [data from Sourjik & Berg (10)]. (b) Nullcline analysis of the dynamical equations for bacterial chemotaxis. The lettered time points (A–E) correspond to those in panel a. The solid gray lines are the Z nullclines, $Z = g(Y, X_1)$ and $Z = g(Y, X_2)$, for different inputs X_1 and $X_2 (> X_1)$, respectively. The horizontal dashed line is the Y nullcline expressed as $F(Z) = 0$, corresponding to a constant value of Z ($Z = Z_s$). The green solid arrow lines show the fast responses caused by changes (addition and removal) of input X between X_1 and X_2 . The blue dashed arrow lines show the slow adaptive dynamics along the Z nullclines. (c) The responses to oscillatory signals are characterized by the response amplitude $|A|$ and the phase shift ϕ . Both dependences of $|A|$ (middle panel) and ϕ (bottom panel) on the input frequency ν quantitatively agree with predictions from the standard model. The results show that the system computes the time derivative of the signal at low frequencies (shaded region), where $\nu < \nu_m \approx 0.006$ Hz. The gradient computation can be seen directly by defining $H \equiv A/(i\nu A_L)$, which remains roughly constant in the shaded region (dashed blue line in the middle panel). Panel c is adapted from Reference 18. Abbreviation: FRET, Förster resonance energy transfer.

as shown in **Figure 2b**. Furthermore, the standard model can be used to predict responses to more complex time-varying signals for direct comparison with quantitative experiments.

3.3.1. Responses to time-varying signals. The standard model has been tested in predicting the responses to ramps and oscillatory signals (see Reference 6 for a recent review). Briefly, by fitting

the measured responses to exponential ramps with the model prediction (18, 20), the intracellular rate function $F(Z)$ can be uniquely determined. Once $F(Z)$ is determined, the standard model can be used to predict responses to any time-varying signals without any adjustable parameters. For an exponentiated sine-wave signal $X(t) = X_0 \exp[A_L \sin(2\pi \nu t)]$, the standard model predicts that the response is $Z(t) = Z_s + \text{Re}(A)$, where the complex response $A = |A| \exp[i(2\pi \nu t - \phi)]$ with the amplitude $|A|$ and a phase delay ϕ is given by

$$|A| = \frac{NZ_s(1 - Z_s)}{\sqrt{1 + (\nu_m/\nu)^2}} A_L, \quad \phi = \pi - \tan^{-1}(\nu_m/\nu), \quad 9.$$

where $\nu_m = -\alpha NZ_s(1 - Z_s)F'(Z_s)/2\pi$ is a characteristic adaptation frequency. The predicted amplitude and phase from Equation 9 agree quantitatively with experiments as shown in **Figure 2c** (18). By taking the Fourier transform of the signal's time derivative $B \equiv i\nu A_L$ and factoring it out from the response, we obtain the systems time-derivative-filtering function $H(\nu) \equiv A/B = NZ_s(1 - Z_s)(i\nu + \nu_m)^{-1}$. As shown in **Figure 2c**, $|H(\nu)|$ is roughly constant for $\nu \ll \nu_m$, which clearly shows that *E. coli* computes time derivatives of the signal at frequencies lower than the adaptation frequency ν_m .

3.3.2. Responses to realistic signals in free-moving cells. Besides predicting responses of immobile cells to prescribed time-varying signals, the standard model has been used to understand intracellular signaling dynamics of free-moving cells (22, 23). The combination of the standard model for the signaling pathway and a quantitative model for the flagellar motor response has yielded significant insights and quantitative predictions on how motile cells behave in spatial-temporally varying environments. These predictions have been tested in microfluidic experiments with stationary, standing-wave, and traveling-wave gradients (24–26).

4. ADAPTATION IN EUKARYOTIC CHEMOTAXIS

Adaptation is not limited to bacterial chemotaxis but is also critically involved in eukaryotic chemotaxis. A number of eukaryotic cells respond to chemical gradients and direct their motion to higher chemoattractant concentrations (27–29). Chemotaxis plays an essential role in several biological processes, including wound healing (30), embryology (31, 32) and cancer cell migration (33). Just as in the case of bacterial chemotaxis, the external chemoattractant molecules bind to surface receptors, activating intracellular signaling pathways that involve a multitude of biochemical components (34). The precise molecular mechanisms for eukaryotic chemotaxis are still under debate (28, 34–36), but many of the pathway components are identified. Furthermore, these pathways are mostly conserved across different cell types, making it possible to use experimentally accessible model systems (37–39). One of the best-studied model systems is *D. discoideum*, a social amoeboid that uses chemotaxis to form aggregation centers following starvation (40, 41). *Dictyostelium* cells move fast and are relatively easy to manipulate in a laboratory setting. Furthermore, many fluorescent reporters are available, making it possible to quantify response kinetics and amplitudes.

How do eukaryotic cells employ chemotaxis? Just like bacteria, eukaryotic cells are able to adapt themselves to their changing surroundings as they move up the gradient. The logic is the same as for bacteria: With an adaptive approach, cells can maintain their responsiveness over a wider range of background concentrations (42, 43). Nevertheless, there are a number of important differences between bacterial chemotaxis and chemotaxis in eukaryotes. These differences are primarily due to the contrasting modes of motion between the two cell types as well as their size disparities. Instead of swimming, eukaryotic cells crawl and migrate by extending their membrane at the front of the cell while retracting the back of the cell (27, 44, 45). The resulting migration speed

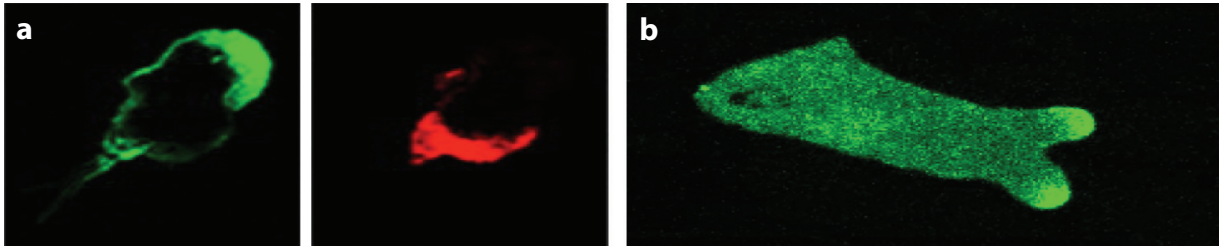


Figure 3

(a) Example of spatial asymmetry breaking in a neutrophil exposed to a gradient (toward the *upper right*). Shown are the distribution of actin (*left*) and phosphorylated myosin light chain (*right*) as revealed by fluorescent staining. Adapted from Reference 53 with permission. (Copyright 2009. The American Association of Immunologists, Inc.) (b) Spatial symmetry breaking in a *Dictyostelium* cell in a gradient pointing to the right. The localization of activated Ras (RasGTP) is visualized using a Ras-binding domain fused to green fluorescent protein (RBD-GFP).

can range from less than 1 $\mu\text{m}/\text{min}$ for macrophages and fibroblasts (46, 47) to approximately 10 $\mu\text{m}/\text{min}$ for neutrophils and *Dictyostelium* cells (48, 49), which is considerably slower than the typical swimming speed of bacteria ($\sim 25 \mu\text{m}/\text{s}$; 2). Chemotaxing eukaryotic cells are, in general, also much larger than bacteria and their 2- μm size, ranging from 10 μm in diameter (neutrophils and *Dictyostelium*) to roughly 100 μm for elongated fibroblasts. Taken together, the much smaller speed and larger cell sizes preclude eukaryotic cells from using the time measurement mechanisms employed by swimming bacteria. Instead, these cells use spatial directional sensing mechanisms, in which the cell's symmetry is broken, leading to a distinct back and front that can be visualized using fluorescent markers (Figure 3) (50–52).

How might adaptation help eukaryotic cells during chemotaxis? Several experimental studies have shown that cells can detect very small gradients (54). For example, *Dictyostelium* cells can respond to concentration differences of approximately 1% across the cell body (55, 56). In addition, these cells respond to gradients with a large range of background concentrations, defined here as the spatially averaged concentration experienced by a cell. Thus, cells cannot determine their direction based on a fixed operating point as this would make them responsive only over a very small concentration range. Instead, cells must be able to compare bound receptor levels at their front and back independent of the background concentration. As suggested by several studies, this comparison will be facilitated by adaptation that ensures that the difference between front and back is independent of background levels (57–59). Importantly, experiments monitoring FRET between two subunits of the receptors have demonstrated that this adaptation occurs downstream from the chemoattractant receptors (60).

4.1. Experimental Evidence for Adaptation

Early experiments, using observations of morphological changes or cell population assays, have suggested that cells can adapt to changing stimuli (61, 62). A more quantitative analysis of adaptation has been made possible by the recent introduction of microfluidics, coupled to improved microscopy. These experimental techniques make it possible to study the dynamics of markers in single cells exposed to carefully controlled environments (48, 52, 56, 63–67). Recently, the dynamics of activated Ras, Ras guanosine triphosphate (RasGTP), was measured using the fluorescent reporter Ras-binding domain fused to green fluorescent protein (RBD-GFP) (68, 69) following step stimuli of chemoattractant. This signaling component was chosen because it is immediately downstream from the G protein-coupled chemoattractant receptors, with Ras likely activating a

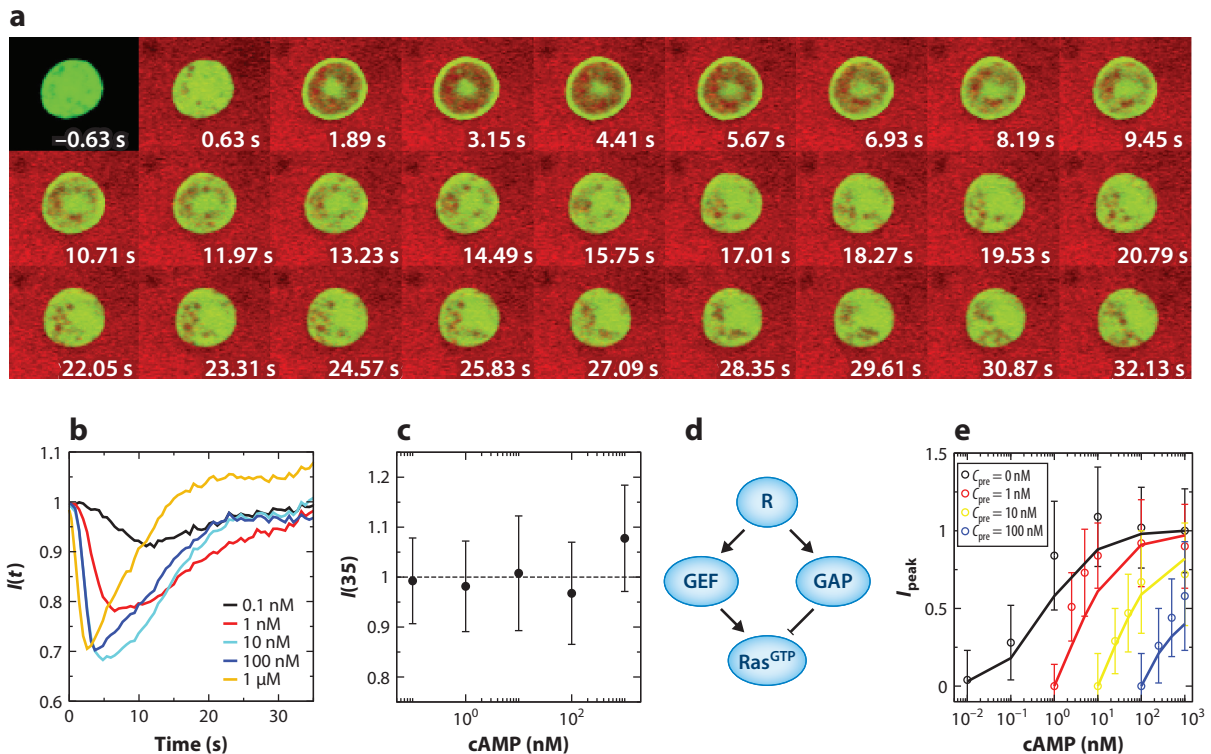


Figure 4

Adaptation measured in *Dictyostelium* cells. Adapted from Reference 68 with permission. (a) Snapshots of a cell undergoing a sudden increase in chemoattractant concentration at $t = 0$ s (visualized in red). Activated Ras is visualized using RBD-GFP, which shows a transient translocation to the membrane. (b) The RBD-GFP cytosolic fluorescence intensity, $I(t)$, normalized by the fluorescence intensity before stimulation, as a function of time for different amounts of stimulation. Note that the time for peak response decreases when the stimulus strength increases. (c) The RBD-GFP cytosolic fluorescence intensity as a function of stimulus strength shows perfect adaptation. (d) Incoherent feed-forward network topology consistent with experimental data: chemoattractant binds to receptors R, which activate both RasGEF and RasGAP. These two enzymes then activate (GEF) and inactivate (GAP) Ras. (e) Experimental results (RBD-GFP dose-response curves, symbols) and the results of the incoherent feed-forward network using model parameters obtained by fitting (lines). The results are plotted in terms of the maximum decrease in cytosolic RBD-GFP fluorescence, I_{peak} , for different pretreatment concentrations, C_{pre} . Abbreviations: GAP, GTPase-activating protein; GEF, guanine nucleotide exchange factor; RBD-GFP, Ras-binding domain–green fluorescent protein.

range of downstream effectors. Thus, its response should be a more direct readout of adaptation than components that are further downstream and which can be part of multiple feed-forward and feedback loops.

Takeda et al. (68) found that without a change in the external cAMP (cyclic adenosine monophosphate) concentration, RBD-GFP is found to be uniformly distributed in the cytosol (Figure 4a). Upon a sudden increase in external cAMP concentration, however, RBD-GFP rapidly localizes to the membrane, followed by a gradual return to the cytosol (Figure 4b). Ras dynamics was quantified following concentration increases of several orders of magnitude (0.1 nM to 1 μ M), and cytosolic RBD-GFP was found to return to its prestimulus level after approximately 35 s, indicating perfect adaptation (Figure 4c). Furthermore, as can be observed from Figure 4b, the time of the peak response decreases for increasing concentration changes. Similar qualitative behavior

was found in a study by Wang et al. (70), which examined the dynamics of PI3K (phosphoinositide 3-kinase) activation using a fluorescent phosphatidylinositol 3,4,5-trisphosphate (PIP3) specific biosensor following a step change in cAMP.

4.2. Network Topology for Adaptation in Eukaryotic Chemotaxis

The finding that activated Ras dynamics adapts perfectly suggests that one of the two basic network motifs described above and shown in **Figure 1b** (NFL or IFFL) should be at the heart of the signaling network. Indeed, the quantitative data from the Takeda et al. experiment allows ruling out the NFL network and is consistent only with the IFFL motif. This can be most readily seen by examining the dynamics of the adaptation as a function of stimulus size. For the NFL motif, the timescales of reaching the maximum response and the subsequent return to basal levels increase (sometimes significantly) as the stimulus size is increased. This can be intuitively understood by realizing that the NFL motif works through a feedback loop. Consequently, a larger stimulus results in larger deviations from equilibrium, requiring more time to return to basal levels.

However, for the IFFL motif the response time can actually decrease upon increasing stimulus strength. This can be seen by analytically examining the dynamics of the response as a function of stimulus strength using simple zero-order forms for the output Z and the internal variable Y :

$$\begin{aligned}\frac{dZ}{dt} &= k_Z X (1 - Z) - k_{-Z} Y Z, \\ \frac{dY}{dt} &= k_Y X - k_{-Y} Y.\end{aligned}\tag{10}$$

The steady-state values are $Y_s = k_Y X / k_{-Y}$ and $Z_s = (k_{-Y} k_Z) / (k_{-Y} k_Z + k_Y k_{-Z})$, illustrating that Z_s is independent of X , the hallmark of perfect adaptation. To approximate the dynamics of recovery, we assume that activation is much faster than inhibition so that we can use the quasi-steady approximation resulting in

$$\frac{1}{X} \frac{dZ}{dt} = k_Z (1 - Z) - \frac{k_Y k_{-Z}}{k_{-Y}} Z.\tag{11}$$

Thus, the recovery timescale increases with X , which is consistent with the experimental results.

To further determine whether the incoherent feed-forward topology is consistent with the experiments, Takeda et al. fitted the experimental data to a model containing an IFFL motif. The model is based on the biochemistry of Ras: Ras is activated by RasGEFs (guanine nucleotide exchange factors) and inactivated by RasGAPs (GTPase activating proteins). Thus, in the adaptation scheme of **Figure 1**, RasGAP is the equivalent of “ Y ”, activated Ras is the equivalent of “ Z ”, and the chemoattractant concentration plays the role of “ X ” (see also **Table 1**). To account for the role of RasGEF, an additional node between the chemoattractant concentration and activated Ras (i.e., X and Z) was inserted. In addition, receptor kinetics was incorporated using experimentally determined values for the binding dynamics. The resulting topology, shown in **Figure 4d**, has the same qualitative features as the IFFL motif of **Figure 1**. The output of the model was tested using a subset of experimental data points, and the values of the parameters were adjusted using a fitting procedure (68). The final model was able to reproduce all experimental results; for example, the dose-response curves of the model and of the experiments show good agreement (see **Figure 4e**). The experimental curves in this figure were obtained using cells that were exposed to different and constant chemoattractant concentrations for prolonged times (denoted by C_{pre}). Other comparisons, involving full time traces and sudden decreases of cAMP concentrations, also show satisfactory agreement between experiment and model, indicating that the IFFL motif is responsible for adaptation.

A similar conclusion was reached by Wang et al., who used a different stimulus protocol to distinguish between the two possible network motifs. Specifically, they used a linear ramp signal $X = X_0 + \beta t$, where β represents the increase in chemoattractant concentration per unit time. Their experiments show that PI3K activity adapts, independent of the value of β (70). This experimental finding is consistent with the IFFL network, for which it is possible to obtain an exact expression for Y as a function of time:

$$Y(t) = \frac{k_Y}{k_{-Y}} \left[X_0 + \beta t + \frac{\beta}{k_{-Y}} (e^{-k_{-Y} t} - 1) \right]. \quad 12.$$

Thus, for large t , both Y and X will increase linearly and will be proportional to the slope of the signal ramp. Therefore, the output Z will not depend on the signal and will adapt perfectly. Note, however, that in general this adaptation is slower than when a step stimulus is applied. In contrast, the NFL motif does not adapt in response to a linear ramp. Thus, combined with the study of Takeda et al., these results imply that adaptation in eukaryotic and bacterial chemotaxis operate using different mechanisms: IFFL for eukaryotes and NFL for bacteria.

4.3. Connection to Directional Sensing Models

Even though the topology of the chemotactic pathway was found to be different than the well-established bacterial chemotaxis pathway, its discovery was not a complete surprise because it was already incorporated into proposed models for eukaryotic chemotaxis. These models do not only have to deal with the response to uniform concentration changes but they also need to explain the spatial asymmetry observed when cells are placed in a gradient (see **Figure 3**). One of the early models for directional sensing is the local excitation, global inhibition (LEGI) model, originally proposed by Parent & Devreotes (57). It contains the IFFL topology and assumes that excitation occurs locally and rapidly and that inhibition is slower and more global, modeled by including a diffusive term for the inhibitor (GAP in **Figure 4d**). The main idea here is that the inhibitor will cancel out the effect of the average receptor occupancy, whereas the local excitation will allow for response to local variations away from the mean (58). Adaptation will then result in a larger response at the side of the cell that is directed toward, rather than to the side pointed away from, the chemoattractant source.

Even though the LEGI model displays perfect adaptation and creates a spatial asymmetry in the presence of a chemoattractant gradient, it is not able to fully capture eukaryotic chemotaxis. The problem is that the generated asymmetry is always smaller than the asymmetry from the gradient. In other words, the LEGI mechanism is not able to amplify an external signal and, instead, simply reads off the external gradient. Several models have been proposed to provide the necessary amplification. For example, a variant of the LEGI model incorporates the idea of zeroth-order ultrasensitivity (71). It no longer assumes that the enzymes that control the readout component are unlimited, resulting in a reaction that is modeled by the full Michaelis–Menten kinetics. Then, for certain parameter values, the readout component of the network can rapidly switch between a low and high state, resulting in the desired amplification (72). Another gradient-sensing model uses a modular approach and postulates that the output of a LEGI module feeds into an excitable module (73, 74). A model cell placed in a gradient will produce a LEGI response that is higher at the front than at the back of the cell. Carefully choosing the model parameters results in excitations that occur more frequently at the front of the cell. Obviously, this model is still able to adapt perfectly and can generate a large response owing to its excitable nature. The fact that cell responses can be described by excitable features was also noted by other studies

(75–78) and is motivated by the transient and stochastic protrusions and retractions of membrane extensions of cells as well as the signaling “patches” following cAMP stimulation (79, 80).

4.4. Scale-Invariant Adaptive Response

In addition to being perfectly adaptive, the response of the LEGI model to sudden stimulus changes can also be scale invariant. A response is said to be scale invariant if its dynamics depends solely on the ratio between the pre- and poststimulus level. In other words, scale invariance implies that a stimulus change from X_0 to X_1 gives the same response as a stimulus change from pX_0 to pX_1 . Such a “fold-change detection” has been investigated theoretically (81–83) and has been demonstrated experimentally in *E. coli* chemotaxis (84). In a more recent study, general necessary and sufficient rules for scale invariance were obtained for three-node network topologies (85). Furthermore, this study investigated whether the topology found in Reference 68 (and shown in **Figure 4b**) exhibits scale invariance. Examining the basic IFFL model of Equation 10 reveals that it is not perfectly scale invariant: Changing the input $X \rightarrow pX$ in the core model will lead to $Y \rightarrow pY$. The equation for the output, however, shows that Z depends nontrivially on both X and Y , leading to dynamics that is not scale invariant. However, in the limit where the output dynamics is very fast, we can use the quasi-steady state approximation. Then, Z is given by its steady-state value, which can be easily verified to be invariant under a fold change in the input.

The full adaptation model, detailed in Reference 68, only displays scale invariance for intermediate values of cAMP stimuli. This is shown in **Figure 5**, where we plot the response of the full model, measured as the level of RBD-GFP, to various changes in external cAMP concentrations. For intermediate values of cAMP, the curves for 1–10 nM and 2–20 nM steps are nearly indistinguishable, indicating scale invariance (**Figure 5b**; see also Reference 85). For smaller and for larger values of cAMP, however, the response is no longer scale invariant, as can be seen in **Figure 5a,c**. The reason for the absence of scale invariance for small values of cAMP is that the steady-state approximation breaks down (for an in-depth discussion of the necessary conditions for scale invariance, we refer to Reference 85). By contrast, for large values of cAMP, the equation of the receptor occupancy in the full model is no longer linearly dependent on the chemoattractant concentration because of receptor saturation. The resulting nonlinear dependence on the cAMP concentration

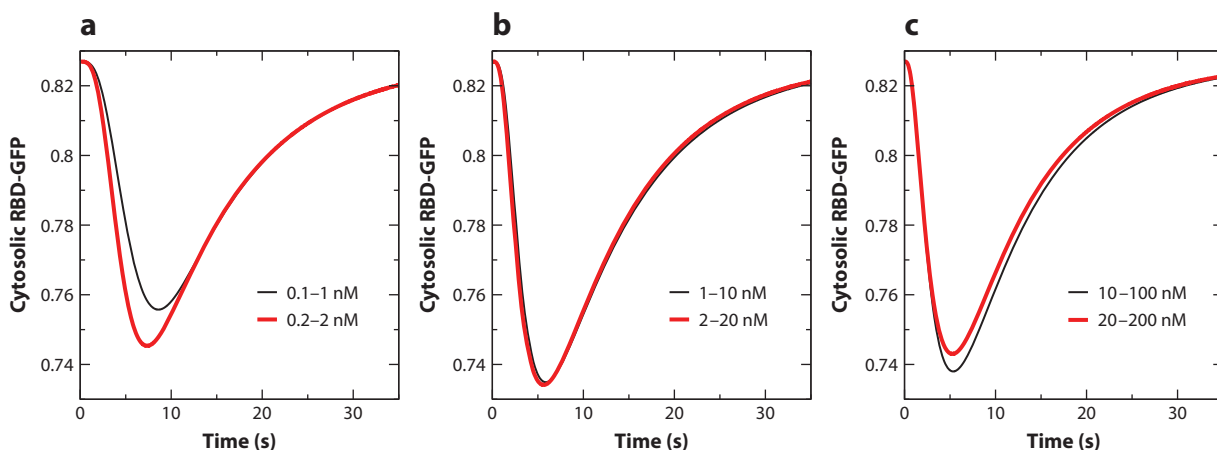


Figure 5

Response of the adaptation model of Reference 68 to different stimulus steps. Only the responses in panel *b* are precisely scale invariant.

leads to responses that are not scale invariant. These model predictions should be testable using the microfluidics system of Takeda et al. in which the concentration is stepped systematically.

5. THE EFFECT OF ADAPTATION: THE WEBER-FECHNER LAW

Why is adaptation so essential in biology? The general answer is that adaptation allows a living system to function normally in a wide range of backgrounds. For sensory systems, this qualitative explanation is related to the well-known empirical Weber–Fechner (WF) law, which states that the response (or perception) of an adaptive sensory system is proportional to the relative change in stimulus. In the following, we describe a general scaling theory for adaptive response to demonstrate the WF law.

5.1. A General Scaling Theory for Adaptive Response

As we discussed in Section 2, for a system adapted to an external stimulus level X , the fast response to a sudden change of stimulus to $X + \Delta X$ can be obtained by assuming that the internal variable Y remains roughly unchanged $Y \approx Y_s(X)$ due to its relatively slow dynamics. Based on the general observation that the primary effect of adaptation is to shift the response curve without changing its shape, we hypothesize that adaptation mainly normalizes the input by a scaling factor $K[Y_s(X)] \equiv K_s(X)$. The peak value can then be written as

$$Z_p(X + \Delta X, X) \approx R \left\{ \frac{X + \Delta X}{K[Y_s(X)]} \right\} \equiv R \left[\frac{X + \Delta X}{K_s(X)} \right], \quad 13.$$

where R is the response function and $K_s(X)$ is the scaling factor that depends on the background X through its direct dependence on Y_s .

The adapted output $Z_s(X)$ at the background level X is given by $Z_s(X) = R[X/K_s(X)]$, from which we can compute the sensitivity S :

$$S(X) \equiv \left| \frac{\Delta Z}{\Delta X} \right| \equiv \left| \frac{Z_p(X + \Delta X, X) - Z_s(X)}{\Delta X} \right| = K_s(X)^{-1} R'[X/K_s(X)], \quad 14.$$

where R' is the derivative of R .

In order to adapt over a wide range of backgrounds, the scaled stimulus strength $X/K_s(X)$ should remain approximately constant for a wide range of X . To satisfy this condition, K_s needs to depend roughly linearly on X :

$$K_s(X) \approx K_0 + \lambda X, \quad 15.$$

where K_0 and λ are constants. Perfect adaptation corresponds to $K_0 = 0$, where the adapted output $Z_s(X) = R(\lambda^{-1})$ is independent of X . The case of no adaptation corresponds to $\lambda = 0$, where K_s does not change with X .

By using Equation 15 for $K_s(X)$, we can compute the sensitivity from Equation 14:

$$S(X) = (K_0 + \lambda X)^{-1} R' \left(\frac{X}{K_0 + \lambda X} \right) \rightarrow C_0 X^{-1} \quad 16.$$

for $X \gg K_0/\lambda$ with $C_0 \equiv \lambda^{-1} R'(\lambda^{-1})$ being a constant. From Equation 16, we have $|\Delta Z| = C_0 \frac{|\Delta X|}{X}$, which is exactly the WF law.

The WF law dictates that the sensory response only depends on the relative change of the stimulus, which is related to the fold-change detection idea that has been studied recently in both bacterial chemotaxis (84) and eukaryotic chemotaxis (68, 85), as discussed in the previous

section. Here, we find that the WF law holds regardless of details of the specific system such as its response function R as long as the scaling hypothesis (Equation 13) and the condition for K_s variation (Equation 15) hold.

5.2. The Weber-Fechner Law in Different Sensory Systems

Next, we show the validity of the scaling hypothesis in both bacterial chemotaxis and eukaryotic chemotaxis and how the WF law can be applied to study adaptive sensory systems in general.

5.2.1. Bacterial chemotaxis. As described in Section 3, an *E. coli* cell adapts to an environment with background chemical concentration X by adjusting its chemoreceptor methylation level to $Y_s(X)$, which restores its preferred activity Z_s . When the concentration changes suddenly to a new level $X + \Delta X$, the immediate response is given by Equation 7. Within the range of receptor sensitivity $K_i \ll X \ll K_a$, we can simplify Equation 7:

$$Z_p(X + \Delta X, X) = \left\{ 1 + \left[\frac{X + \Delta X}{K_s(X)} \right]^N \right\}^{-1}, \quad 17.$$

which satisfies the scaling hypothesis of Equation 13 with the response function R taking the form of a Hill function with a Hill coefficient N . By determining Y_s using the perfect adaptation condition $Z_p(X, X) = Z_s$, the scaling factor is given by $K_s(X) = K_i \exp[\alpha(Y_s - m_0)] = (Z_s^{-1} - 1)^{\frac{1}{N}} X$, which depends linearly on X , confirming the condition of Equation 15 for perfect adaptation. By using the expression for $K_s(X)$ in Equation 14, we can determine the sensitivity:

$$S(X) \approx NZ_s(1 - Z_s)X^{-1}, \quad 18.$$

which is valid for $X \gg K_i$. Equation 18 is exactly the WF law in bacterial chemotaxis.

For a nonadaptive mutant cell, e.g., a cell with its receptor methylation level fixed, the scaling factor K_s remains a constant independent of the input X : $K_s(X) = K_{na}$. From Equation 14, the sensitivity for nonadaptive cells can be computed $S_{na}(X) \approx NK_{na}^N X^{-(N+1)}$ for $X \gg K_{na}$, which decays much faster than that for the adaptive cell given in Equation 18.

5.2.2. Eukaryotic chemotaxis. For eukaryotic chemotaxis, adaptation is achieved by an IFFL network, the dynamics for which are described by Equation 10. We can compute the response by first using the quasi-equilibrium condition to determine the internal variable $Y_s \approx \frac{k_Y}{k_{-Y}} X$ at a background X . After the input changes from X to $X + \Delta X$, the output Z starts to increase and the peak response can be found by setting $dZ/dt = 0$ in Equation 10, which results in

$$Z_p(X + \Delta X, X) \approx \frac{k_Z(X + \Delta X)}{k_Z(X + \Delta X) + k_{-Z}Y_s} = \frac{u}{u + 1}, \quad 19.$$

where $u = (X + \Delta X)/K_s(X)$. The scaling factor $K_s(X) = k_{-Z}k_Z^{-1}Y_s = \frac{k_{-Z}k_Y}{k_{-Y}k_Z} X$ depends linearly on X in agreement with the perfect adaptation condition in Equation 15. The sensitivity at background X can be easily determined:

$$S(X) = (1 - Z_s)Z_s X^{-1}, \quad 20.$$

which follows the WF law. For nonadaptive mutants with a fixed Y , it is easy to show that the sensitivity decays as X^{-2} , which is faster than that of the WT cells.

From Equations 18 and 20, we show that the scaling hypothesis for adaptive response holds, and the WF law is universal for adaptive systems independent of the underlying biochemical network structure (NFL or IFFL).

5.2.3. Sensory neurons. The general scaling model for adaptive response can be used to describe adaptive systems even in cases in which the detailed adaptation mechanisms are not fully understood. The functional form of the response function R can be measured by nonadaptive mutants in which K_s remains a constant independent of the background. Once R is determined, then all responses of the adaptive WT cells in a given background can be determined by just two parameters, K_0 and λ . This approach has been used successfully to explain response sensitivities in both the rhodopsin and the olfactory neurons (86).

6. NONEQUILIBRIUM THERMODYNAMICS OF ADAPTATION

Inside a living cell, all biological functions are carried out by biochemical reactions with a relatively small number of molecules (much smaller than Avogadro's number). The stochastic nature of molecular reactions and diffusion gives rise to significant fluctuations in biochemical reactions. Another general feature of living systems is that they are far from equilibrium. Living matter is highly dissipative. Chemical free energy harvested by metabolic processes powers interactions of living matter in different biochemical networks to achieve various biological functions. How do we describe the nonequilibrium thermodynamics of a small living system? How can a cell function accurately in the face of these noisy biochemical reactions? In the following, we address these questions in the context of cellular sensory adaptation.

6.1. Breakdown of Detailed Balance

To understand the effect of noise in adaptation dynamics, we introduce the Langevin dynamics by including noise in the simple dynamical equations described in Section 2:

$$\frac{dZ}{dt} = G(X, Y, Z) + \eta_Z, \quad \frac{dY}{dt} = F(X, Y, Z) + \eta_Y, \quad 21.$$

$$\langle \eta_Z(t + t') \eta_Z(t') \rangle = \Delta_Z \delta(t), \quad \langle \eta_Y(t + t') \eta_Y(t') \rangle = \Delta_Y \delta(t), \quad 22.$$

where η_Y and η_Z are noise terms due to the stochastic nature of the underlying biochemical reactions. In general, the noise strength Δ_Y and Δ_Z can depend on the variables (X, Y, Z) .

For an equilibrium system with an energy functional $\mathcal{E}(X, Y, Z)$, its dynamics is driven by the local gradient of $\mathcal{E}(X, Y, Z)$ in addition to thermal fluctuations. For example, in its simplest form, we can have $G = -\frac{\partial \mathcal{E}}{\partial Z}$, and $F = -\frac{\partial \mathcal{E}}{\partial Y}$ with the noise strength $\Delta_Y = \Delta_Z = 2k_B T$, where $k_B T$ is the thermal energy of the heat bath with which the system is in equilibrium. It is easy to show that the equilibrium Langevin equation leads to the Boltzmann distribution $\exp(-\frac{\mathcal{E}}{k_B T})$. Independent of the specific form of $\mathcal{E}(X, Y, Z)$, the constraint $\frac{\partial G}{\partial Y} = \frac{\partial F}{\partial Z}$ is satisfied by all equilibrium systems as a result of the detailed balance (87).

However, as we discussed in Section 2, in adaptive systems these two cross derivative terms ($\frac{\partial G}{\partial Y}$ and $\frac{\partial F}{\partial Z}$) have different signs and thus cannot be equal:

$$\frac{\partial G}{\partial Y} \neq \frac{\partial F}{\partial Z}, \quad 23.$$

which means that detailed balance is violated in adaptation, and the underlying biochemical reactions are driven out of equilibrium by energy dissipation.

6.2. The Energy–Speed–Accuracy Trade-Off

How does the system use free energy to achieve adaptation, and how does the energy dissipation relate to and limit the performance of adaptation? To answer these questions, we investigate

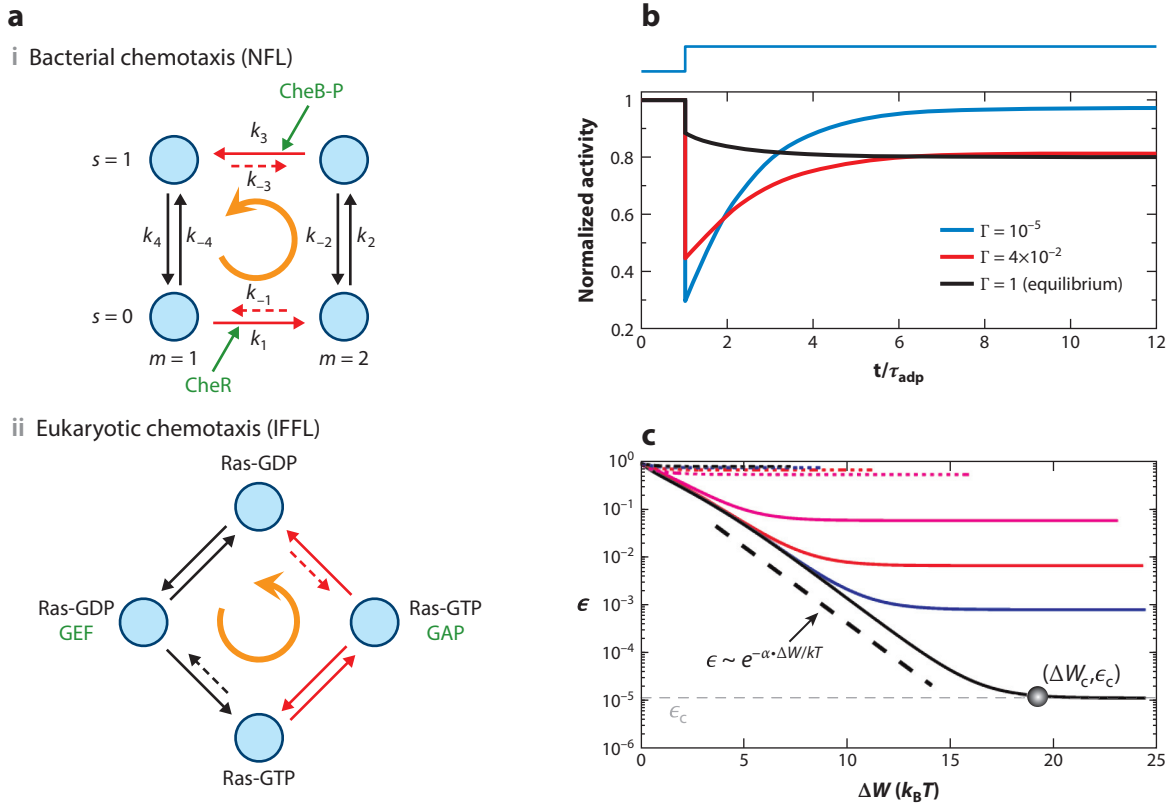


Figure 6

The nonequilibrium dynamics in adaptation and the universal energy–speed–accuracy trade-off. (a) Biochemical reactions in (i) the NFL and (ii) the IFFL networks for adaptation. Both biochemical networks break detailed balance and persistent flux cycles, as illustrated by the orange cycling arrows, exist in the adapted nonequilibrium steady state (NESS). The fast and slow reactions are distinguished by the black and red arrows, respectively. The key enzymes that facilitate the nonequilibrium reaction cycles are highlighted in green. Reactions suppressed by free-energy dissipation are labeled by dotted arrows. (b) No adaptations exist for the equilibrium model with $\Gamma = 1$ (black line). Adaptive dynamics occurs after Γ decreases beyond a certain critical value and it becomes more accurate as Γ decreases (red and blue lines). (c) The energy–speed–accuracy relationship. The adaptation error ϵ decreases exponentially with $\Delta W \propto |\ln \Gamma|$ until it reaches a saturation value ϵ_c , which depends on specific parameters of the system as well as the background signal level. Different lines correspond to different background attractant concentrations. Panels b and c are adapted from Reference 88.

the key biochemical reactions underlying the two adaptation circuit motifs—NFL and IFFL—as shown in **Figure 6a**.

For adaptation in *E. coli* chemotaxis, each state of the chemoreceptor is characterized by a pair of order parameters (s, m) : $s = 0, 1$ corresponding to the active and inactive states of the receptor, respectively, and the receptor methylation level $m = 1, 2$ (only two adjacent levels are considered here). The biochemical transition rates between the four states are given in **Figure 6a(i)** with all the counterclockwise (CCW) and clockwise (CW) rates labeled by k_l and k_{-l} , respectively ($l = 1, 2, 3, 4$).

For a fixed receptor methylation level, the transitions between the active and inactive states of the receptor are governed by the free-energy levels of the two states; i.e., $\frac{k_2}{k_{-2}} = \exp[E(0, 2) - E(1, 2)]$, $\frac{k_4}{k_{-4}} = \exp[E(1, 1) - E(0, 1)]$, where $E(s, m) = sf_m(m)$ is the free-energy level of state

(s, m) with $f_m(m) = -\alpha(m - m_0)$ the methylation free energy (see Section 3). The rates for receptor methylation and demethylation, however, do not satisfy detailed balance. In particular, in order to carry out negative feedback control, the methylation rate for the inactive receptor should be enhanced relative to the demethylation rate, and the demethylation rate should be increased relative to the methylation rate for the active receptor; i.e., $\frac{k_1}{k_{-1}} > \exp[E(0, 1) - E(0, 2)]$ and $\frac{k_3}{k_{-3}} > \exp[E(1, 2) - E(1, 1)]$. These two nonequilibrium processes are facilitated by two enzymes—CheR for methylation and CheB-P for demethylation reactions.

We can define a “reversibility” parameter Γ for the whole reaction cycle,

$$\Gamma \equiv \frac{\prod_{\text{ccw}} k}{\prod_{\text{cww}} k} = \prod_{l=1}^4 \frac{k_{-l}}{k_l}, \quad 24.$$

which determines whether the full reaction cycle is in thermal equilibrium with its environment. For $\Gamma \neq 1$, the system is dissipative and its steady state is a nonequilibrium steady state (NESS), which needs to be maintained by a finite rate of free-energy consumption.

For the adaptation network in *E. coli*, the negative feedback control is carried out by suppressing the “undesirable” backward reactions, which can be characterized by a small parameter $\gamma < 1$: $k_{-1} = \gamma k_{-1}^{(0)}$ and $k_{-3} = \gamma k_{-3}^{(0)}$, where the equilibrium backward rates $k_{-1}^{(0)}$ and $k_{-3}^{(0)}$ satisfy detailed balance with their corresponding forward rates, resulting in an irreversible parameter $\Gamma = \gamma^2$. For an equilibrium system with $\Gamma = 1$, the system does not adapt (see **Figure 6b**). Adaptation only occurs when Γ decreases below a critical value $\Gamma_c < 1$. The adaptation error decreases as Γ decreases below Γ_c . The adaptation error can be expressed as: $\epsilon = \epsilon_c + \epsilon_0 \gamma$, where ϵ_0 is an $O(1)$ constant that depends on details of the system. The saturation error at $\gamma \rightarrow 0$ is given by ϵ_c , which depends on other system parameters. ϵ_c can be made arbitrarily small by proper design of the system (88). For those systems with $\epsilon_c \approx 0$, perfect adaptation ($\epsilon = 0$) can be achieved when $\gamma = 0$.

The entropy production rate of the system can be computed: $\dot{S} = \sum_l (J_{l+} - J_{l-}) \ln(J_{l+}/J_{l-})$, where $J_{l\pm}$ are the forward and backward probability fluxes for the l th reaction. From \dot{S} , we can determine a minimum free-energy dissipation rate $\dot{W} = k_B T \dot{S}$ to maintain the adapted state, where the thermal energy unit $k_B T$ of the environment can be set to unity. It can be shown that the dissipation rate increases with the adaptation speed $\omega_{\text{adp}} \equiv \tau_{\text{adp}}^{-1}$ with τ_{adp} the adaptation time: $\dot{W} = -c_0 \omega_{\text{adp}} \ln(\gamma)$, with c_0 a system dependent $O(1)$ constant.

By varying γ , i.e., the strength of the negative feedback control, we can relate the cost of adaptation as characterized by the minimum free-energy dissipation rate (\dot{W}) with its performance characterized by its speed (ω_{adp}) and accuracy (ϵ):

$$\dot{W} = c_0 \times \omega_{\text{adp}} \times \ln \left(\frac{\epsilon_0}{\epsilon - \epsilon_c} \right), \quad 25.$$

which is called the energy–speed–accuracy (ESA) trade-off relationship as shown in **Figure 6c**.

The ESA relationship seems to be general for adaptive systems. Equation 25 was found to be valid for the IFFL network in eukaryotic chemotaxis (89). Similar to adaptation by negative feedback control in bacterial chemotaxis, two opposing enzymes, GEF and GAP, activate and deactivate Ras, respectively, through two different paths in eukaryotic chemotaxis as shown in **Figure 6a(ii)**. Free energy is continuously consumed in the adapted steady state to suppress the “undesirable” reverse reactions and drive a sustained cycling flux among the four states.

The free energy is provided by the hydrolysis of high-energy biomolecules that are coupled with these cycles, e.g., ATP or GTP for the phosphorylation–dephosphorylation cycle in eukaryotic chemotaxis and S-adenosylmethionine (SAM) for the methylation–demethylation cycle in bacterial chemotaxis. Measurements of the adaptation dynamics in energy-deprived *E. coli* cells are consistent with the ESA relationship (88).

The general ESA relationship provides a fundamental physical limit for an important biological function: adaptation. It also provides insights into designing biochemical circuits to achieve optimal performance with limited resources. The effect of energy dissipation on other key characteristics of adaptation has also been studied. In particular, free-energy dissipation was found to suppress fluctuation of the adapted activity without affecting the short time response of the system, a violation of the fluctuation dissipation relationship in equilibrium systems (90).

7. ADAPTATION IN OTHER BIOLOGICAL SYSTEMS

Adaptation in cells is not limited to chemotaxis signaling. For example, it was recently found that the bacterial flagellar switch can adapt to the intracellular CheY-P level by adjusting the number of FliM molecules at the switch complex (91, 92). Adaptation also plays a key role in a variety of homeostatic processes, e.g., adaptation to hyperosmotic shocks in budding yeast *Saccharomyces cerevisiae* cells. In a recent study, Muzzey et al. measured nuclear enrichment of the MAP kinase Hog1 and found it to adapt perfectly, meaning that the steady-state pre- and poststimulus levels were identical (93). This study also argued for the presence of an integrator and found, through a set of carefully chosen experiments either in mutant strains or for different stimulus protocols, that a single integrating mechanism that involves Hog1 kinase activity and that regulates glycerol synthesis is responsible for the observed adaptation.

All sensory neurons show adaptive behaviors. Although the full molecular mechanism is unclear, some key steps in the adaptation pathway are known. For example, in olfactory sensing in mammalian neurons (94, 95), odorant binding induces activation of adenylyl cyclase (AC), which causes an inbound calcium (Ca^{+2}) flux. The intracellular calmodulin (CaM) interacts with enriched calcium to form Ca–CaM, which activates AC phosphorylase calmodulin kinase II (CAMKII) that eventually phosphorylates and deactivates AC. For light sensing in mammalian neurons (96–98), light activates the G–protein coupled receptor (photon sensor) that decreases the cellular level of cyclic guanosine monophosphate (cGMP) and inhibits the inbound calcium (Ca^{+2}) flux, which eventually turns on the octopus rhodopsin kinase (ORK) to phosphorylate and deactivate the photon sensor. Finally, the adaptation mechanism for hair cells might involve Ca^{+2} , although this is still controversial (99, 100). All these neuron adaptation examples have the existence of multiple timescales in common. Thus, it is highly likely that a nested network consisting of both NFL and IFFL motifs is employed in neuron adaptation. It should thus be interesting to use the dynamical systems approach described here together with quantitative single-cell measurements to determine the underlying network architecture for adaptation in more complex systems such as sensory neurons.

As a final example of adaptation, we would like to point out that it does not have to be limited to single cells but can also occur at the tissue, organ, or whole-body level. One example of perfect adaptation at the body level can be found in the control of calcium levels in mammals. These levels need to be well controlled and must be within a small range of values. El-Samad et al. described how an integral control feedback mechanism is able to achieve these requirements and proposed a biologically plausible model for calcium homeostasis (101). Specifically, they showed that a previously proposed and simple feedback control mechanism is not sufficient to robustly control

calcium levels and that the addition of an integrator, much like the one schematically shown in **Figure 1**, is able to ensure calcium levels that are independent of the perturbation. When applied to data from cows that give birth, representing a large calcium perturbation, the model was able to capture the perfect adaptation observed in the animals. As one can imagine, however, obtaining large amounts of quantitative data at animal scales is a complicated and time-consuming task, illustrating why chemotaxis of single cells is a favorite system for the study of adaptation.

8. REPRISE

In this paper, we reviewed the two basic molecular mechanisms, NFL and IFFL, for cellular adaptation exemplified by the bacterial and eukaryotic chemotaxis signaling pathways, respectively. Despite their different network architectures, they share many common and universal characteristics in their dynamics, energetics, and scaling behavior. To display adaptive dynamics, both pathways require a separation of timescales with a fast response and a slow recovery. Both operate out of thermal equilibrium, continuously dissipating (consuming) free energy to maintain the adapted steady state. The power consumption sets a limit for the adaptation performance characterized by adaptation speed and accuracy. Adaptation maintains a high sensitivity over a wide range of backgrounds, which is directly responsible for the WF scaling law observed in different sensory systems. There are, however, notable differences in the dynamics of these two networks. Although both the response and the recovery timescales in the IFFL network decrease with the signal strength, they increase with or are independent of the input in the NFL network. These differences can be exploited to determine the underlying molecular mechanism for adaptation from input–output measurements. Indeed, the theoretical framework we described here should be useful to understand more complicated adaptive systems in biology.

SUMMARY POINTS

1. There are two distinct basic biochemical networks that lead to accurate adaptation—the negative feedback loop (NFL) network and the incoherent feed-forward loop (IFFL) network.
2. Both NFL and IFFL networks operate with at least two separate timescales—a fast response time and a slow recovery (adaptation) time.
3. Adaptation in bacterial chemotaxis involves an NFL network motif. Adaptation in eukaryotic chemotaxis involves an IFFL network motif.
4. The timescales in IFFL decrease with the signal intensity, whereas the NFL timescales increase with the signal or show no dependence.
5. A general scaling theory of adaptive response is developed to derive the Weber-Fechner law in both bacterial chemotaxis and eukaryotic chemotaxis systems.
6. Both bacterial chemotaxis and eukaryotic chemotaxis can show scale-invariant responses or fold-change detection due to adaptation.
7. Adaptation costs energy. The adapted state continuously consumes energy to maintain its stability. There is a universal trade-off relationship between the energy dissipation rate and the adaptation speed and accuracy.

FUTURE ISSUES

1. Probing adaptive motifs in complex signaling pathways requires fast and quantifiable perturbation to intracellular components. The recently developed optogenetic methods (102), which use light to reversibly activate specific components within a pathway (103–106), may be employed to decipher pathway topologies.
2. Quantitative experimental techniques, including microfluidics that generate time-varying stimuli (52, 54, 56, 67, 107), can be used together with modeling to determine key model parameters and their cell-to-cell variability.
3. The current modeling framework can be extended to study complex biochemical networks with multiple timescales and nested IFFL and NFL motifs, such as those involved in adaptation in sensory neurons.

DISCLOSURE STATEMENT

The authors are not aware of any affiliations, memberships, funding, or financial holdings that might be perceived as affecting the objectivity of this review.

ACKNOWLEDGMENTS

The work by Y.T. is supported by the National Institutes of Health (NIH) Grant No. R01 GM081747. W.J.R. is supported by NIH Grant No. P01 GM078586. We thank our collaborators for insightful discussions. We apologize to authors in the field whose work is not cited owing to space limitations.

LITERATURE CITED

1. Ma W, Trusina A, El-Samad H, Lim WA, Tang C. 2009. *Cell* 138:760–73
2. Berg HC, Brown DA. 1972. *Nature* 239:500–4
3. Kollmann M, Lvdko L, Bartholom K, Timmer J, Sourjik V. 2005. *Nature* 438:504–7
4. Hazelbauer G, Falke J, Parkinson J. 2008. *Trends Biochem. Sci.* 33:9–19
5. Maddock J, Shapiro L. 1993. *Science* 259:1717
6. Tu Y. 2013. *Annu. Rev. Biophys.* 42:337–59
7. Spiro PA, Parkinson JS, Othmer HG. 1997. *PNAS* 94:7263–68
8. Barkai N, Leibler S. 1997. *Nature* 387:913–17
9. Mello BA, Tu Y. 2003a. *Biophys. J.* 84:2943–56
10. Sourjik V, Berg HC. 2002. *PNAS* 99:123–27
11. Sourjik V. 2004. *Trends Microbiol.* 12(12):569–76
12. Mello B, Tu Y. 2005. *PNAS* 102:17354
13. Keymer JE, Endres RG, Skoge M, Meir Y, Wingreen NS. 2006. *PNAS* 103:1786–91
14. Duke T, Bray D. 1999. *PNAS* 96:10104
15. Mello B, Tu Y. 2003b. *PNAS* 100:8223
16. Mello B, Shaw L, Tu Y. 2004. *Biophys. J.* 87:1578–95
17. Shimizu TS, Delalez N, Pichler K, Berg H. 2006. *PNAS* 103:2093–97
18. Shimizu T, Tu Y, Berg H. 2010. *Mol. Syst. Biol.* 6:382
19. Yi TM, Huang Y, Simon MI, Doyle J. 2000. *PNAS* 97:4649–53
20. Tu Y, Shimizu T, Berg H. 2008. *PNAS* 105:14855
21. Block S, Segall J, Berg H. 1983. *J. Bacteriol.* 154:312–23

22. Jiang L, Ouyang Q, Tu Y. 2010. *PLoS Comput. Biol.* 6:e1000735
23. Si G, Wu T, Ouyang Q, Tu Y. 2012. *Phys. Rev. Lett.* 109:048101
24. Kalinin Y, Jiang L, Tu Y, Wu M. 2009. *Biophys. J.* 96:2439–48
25. Zhu X, Si G, Deng N, Ouyang Q, Wu T, et al. 2012. *Phys. Rev. Lett.* 108:128101
26. Li Z, Cai Q, Zhang X, Si G, Ouyang Q, et al. 2017. *Phys. Rev. Lett.* 118:098101
27. Ridley AJ, Schwartz MA, Burridge K, Firtel RA, Ginsberg MH, et al. 2003. *Science* 302:1704–9
28. Levine H, Rappel WJ. 2013. *Phys. Today* 66(2):10.1063/PT.3.1884
29. Iglesias PA. 2012. *Sci. Signal.* 5:pe8
30. Clark R. 1996. *The Molecular and Cellular Biology of Wound Repair*. New York: Plenum
31. Yu TW, Bargmann CI. 2001. *Nat. Neurosci.* 4:1169–76
32. Montell DJ. 2003. *Nat. Rev. Mol. Cell Biol.* 4:13–24
33. Condeelis J, Singer RH, Segall JE. 2005. *Annu. Rev. Cell Dev. Biol.* 21:695–718
34. Swaney KF, Huang CH, Devreotes PN. 2010. *Annu. Rev. Biophys.* 39:265–89
35. Graziano BR, Weiner OD. 2014. *Curr. Opin. Cell Biol.* 30:60–67
36. Insall RH. 2010. *Nat. Rev. Mol. Cell Biol.* 11:453–58
37. van Es S, Devreotes PN. 1999. *Cell. Mol. Life Sci.* 55:1341–51
38. Jin T, Xu X, Fang J, Isik N, Yan J, et al. 2009. *Immunol. Res.* 43:118–27
39. Artemenko Y, Lampert TJ, Devreotes PN. 2014. *Cell. Mol. Life Sci.* 71:3711–47
40. Kessin RH. 2001. *Dictyostelium: The Evolution, Cell Biology, and Development of a Social Organism*. Cambridge, UK: Cambridge Univ. Press
41. Loomis WF. 1982. *The Development of Dictyostelium discoideum*. New York: Academic
42. Chang H, Levchenko A. 2013. *Philos. Trans. R. Soc. B* 368:20130117
43. Iglesias PA, Shi C. 2014. *IET Syst. Biol.* 8:268–81
44. Lauffenburger DA, Horwitz AF. 1996. *Cell* 84:359–69
45. Pollard TD, Borisy GG. 2003. *Cell* 112:453–55
46. Allen WE, Zicha D, Ridley AJ, Jones GE. 1998. *J. Cell Biol.* 141:1147–57
47. Monypenny J, Zicha D, Higashida C, Ocegüera-Yanez F, Narumiya S, Watanabe N. 2009. *Mol. Cell Biol.* 29:2730–47
48. Jeon NL, Baskaran H, Dertinger SK, Whitesides GM, de Water LV, Toner M. 2002. *Nat. Biotechnol.* 20:826–30
49. Wessels D, Soll DR, Knecht D, Loomis WF, De Lozanne A Spudich J. 1988. *Dev. Biol.* 128:164–77
50. Bourne HR, Weiner O. 2002. *Nature* 419:21
51. Haastert PJV, Devreotes PN. 2004. *Nat. Rev. Mol. Cell Biol.* 5:626–34
52. Skoge M, Adler M, Groisman A, Levine H, Loomis WF, Rappel W-J. 2010. *Integr. Biol. (Camb.)* 2(11–12):659–68
53. Shi Y, Zhang J, Mullin M, Dong B, Alberts AS, Siminovitch KA. 2009. *J. Immunol.* 182:3837–45
54. Herzmark P, Campbell K, Wang F, Wong K, El-Samad H, et al. 2007. *PNAS* 104:13349–54
55. Fisher PR, Merkl R, Gerisch G. 1989. *J. Cell Biol.* 108:973–84
56. Song L, Nadkarni SM, Bödeker HU, Beta C, Bae A, et al. 2006. *Eur. J. Cell Biol.* 85:981–89
57. Parent CA, Devreotes PN. 1999. *Science* 284:765–70
58. Levchenko A, Iglesias PA. 2002. *Biophys. J.* 82:50–63
59. Ming G, Wong ST, Henley J, Yuan Xb, Song H, et al. 2002. *Nature* 417:411–18
60. Janetopoulos C, Jin T, Devreotes P. 2001. *Science* 291:2408–11
61. Zigmond SH, Sullivan SJ. 1979. *J. Cell Biol.* 82:517–27
62. van Haastert PJM, van der Heijden PR. 1983. *J. Cell Biol.* 96:347–53
63. Xu X, Meier-Schellersheim M, Jiao X, Nelson LE, Jin T. 2005. *Mol. Biol. Cell* 16:676–88
64. Xu X, Meier-Schellersheim M, Yan J, Jin T. 2007. *J. Cell Biol.* 178:141–53
65. Sasaki AT, Chun C, Takeda K, Firtel RA. 2004. *J. Cell Biol.* 167:505–18
66. Irimia D, Geba DA, Toner M. 2006. *Anal. Chem.* 78:3472–77
67. Skoge M, Yue H, Erickstad M, Bae A, Levine H, et al. 2014. *PNAS* 111:14448–53
68. Takeda K, Shao D, Adler M, Charest PG, Loomis WF, et al. 2012. *Sci. Signal.* 5:ra2
69. Rappel WJ, Firtel RA. 2012. *Cell Cycle* 11:1051–52
70. Wang CJ, Bergmann A, Lin B, Kim K, Levchenko A. 2012. *Sci. Signal.* 5:ra17

71. Goldbeter A, Koshland DE. 1981. *PNAS* 78:6840–44
72. Levine H, Loomis WF, Rappel WJ. 2010. In *New Perspectives in Mathematical Biology*, ed. S Sivaloganathan, *Fields Inst. Commun.*, pp. 1–20. Providence, RI: Am. Math. Soc.
73. Xiong Y, Huang CH, Iglesias PA, Devreotes PN. 2010. *PNAS* 107:17079–86
74. Iglesias PA, Devreotes PN. 2012. *Curr. Opin. Cell Biol.* 24:245–53
75. Arriumerlou C, Meyer T. 2005. *Dev. Cell* 8:215–27
76. Whitelam S, Bretschneider T, Burroughs NJ. 2009. *Phys. Rev. Lett.* 102:198103
77. Hecht I, Kessler DA, Levine H. 2010. *Phys. Rev. Lett.* 104:158301
78. Cooper RM, Wingreen NS, Cox EC. 2012. *PLOS ONE* 7:e33528
79. Postma M, Roelofs J, Goedhart J, Gadella TW, Visser AJ, Haastert PJV. 2003. *Mol. Biol. Cell* 14:5019–27
80. Nishikawa M, Horning M, Ueda M, Shibata T. 2014. *Biophys. J.* 106:723–34
81. Shoval O, Goentoro L, Hart Y, Mayo A, Sontag E, Alon U. 2010. *PNAS* 107:15995–6000
82. Shoval O, Alon U, Sontag E. 2011. *SIAM J. Appl. Dyn. Syst.* 10:857–96
83. Kamino K, Kondo Y. 2016. *PLOS ONE* 11:e0164674
84. Lazova MD, Ahmed T, Bellomo D, Stocker R, Shimizu TS. 2011. *PNAS* 108:13870–75
85. Skataric M, Sontag ED. 2012. *PLOS Comput. Biol.* 8:e1002748
86. Cao LH, Jing BY, Yang D, Zeng X, Shen Y, et al. 2016. *PNAS* 113:E902–11
87. Van Kampen NG. 2007. *Stochastic Processes in Physics and Chemistry. North-Holland Personal Library.* Amsterdam: Elsevier Sci. 3rd ed.
88. Lan G, Sartori P, Neumann S, Sourjik V, Tu Y. 2012. *Nat. Phys.* 8:422–28
89. Lan G, Tu Y. 2013. *J. R. Soc. Interface* 10:20130489
90. Sartori P, Tu Y. 2015. *Phys. Rev. Lett.* 115:118102
91. Yuan J, Brand RW, Basarab GH, Berg H. 2012. *Nature* 484:233–36
92. Tu Y, Berg HC. 2012. *J. Mol. Biol.* 423:782–88
93. Muzzey D, Gomez-Uribe CA, Mettetal JT, van Oudenaarden A. 2009. *Cell* 138:160–71
94. Kurahashi T, Menini A. 1997. *Nature* 385:725–29
95. Matthews HR, Reisert J. 2003. *Curr. Opin. Neurobiol.* 13:469–75
96. Nakatani K, Tamura T, Yau KW. 1991. *J. Gen. Physiol.* 97:413–35
97. Fain GL, Matthews HR, Cornwall MC, Koutalos Y. 2001. *Physiol. Rev.* 81:117–51
98. Burns M, Baylor DA. 2001. *Ann. Rev. Neurosci.* 24:779–805
99. Peng AW, Effertz T, Ricci AJ. 2013. *Neuron* 80(4):960–72
100. Corns LF, Johnsona SL, Krosb CJ, Marcotti W. 2014. *PNAS* 111:14918–23
101. El-Samad H, Goff JP, Khammash M. 2002. *J. Theor. Biol.* 214:17–29
102. Boyden ES, Zhang F, Bamberg E, Nagel G, Deisseroth K. 2005. *Nat. Neurosci.* 8:1263–68
103. Levskaya A, Weiner OD, Lim WA, Voigt CA. 2009. *Nature* 461:997–1001
104. Toettcher JE, Weiner OD, Lim WA. 2013. *Cell* 155:1422–34
105. Toettcher JE, Voigt CA, Weiner OD, Lim WA. 2011. *Nat. Methods* 8:35–38
106. Wu YI, Frey D, Lungu OI, Jaehrig A, Schlichting I, et al. 2009. *Nature* 461:104–8
107. Fuller D, Chen W, Adler M, Groisman A, Levine H, et al. 2010. *PNAS* 107:9656–59